NUMERICAL STUDY OF PENETRATIVE AND "SOLID-LID" NON-PENETRATIVE CONVECTIVE BOUNDARY LAYERS

Zbigniew Sorbjan
School of Meteorology, University of Oklahoma

Submitted to:
Journal of the Atmospheric Sciences

April 1995

ABSTRACT

A large-eddy simulation model was used to generate and compare statistics of turbulence during non-penetrative and penetrative dry convection. In penetrative convection, dimensionless vertical velocity in updrafts were obtained to have almost the same values as in the non-penetrative case. The counter-gradient transport of heat and moisture was found to be present during non-penetrative convection at $z/z_i > 0.6$. For penetrative convection, the counter-gradient transport of heat occurred only in a layer $0.5 < z/z_i < 0.75$, while the counter-gradient transport of humidity was not present. During non-penetrative convection, temperature and humidity were perfectly correlated. In penetrative convection, the correlation coefficient was found to be less than unity and varying from about 0.9 near the surface to about -0.7 at the top of the mixed layer.

1. INTRODUCTION

Convection occurs in a broad range of forms and scales. It can be observed in a container of heated liquid, as well as in the atmosphere or lake. Convection takes the form of hexagonal cells or horizontal rolls marked sometimes by a presence of clouds in the atmosphere (e.g., Agee, 1987), or it is exhibited as foam patterns on lake surfaces. During the last three decades, laboratory and numerical research have led to the accumulation of qualitative and quantitative knowledge of atmospheric convection.

Basic aspects of convection were explored with the convection tank (e.g., Deardorff et al., 1969; Willis and Deardorff, 1974; Deardorff et al., 1980; Adrian et al., 1986, Kumar and Adrian, 1986). An important portion of the present understanding of the convectively mixed layer was achieved through numerical simulations, first through "large-eddy simulations" (LES), and later through “direct numerical simulations” (DNS). The advantage of such simulations is based on the fact that both LES and DNS use equations that are derivable from the exact set and, hence remain faithful to the essential physics of the flow (e.g., Nieuwstadt, 1990, Wyngaard, 1992; Mason, 1994). The first numerical large-eddy simulations were performed by Deardorff (1972, 1973 a, b, 1974). Large-eddy simulations of atmospheric convection were later investigated by e.g., Schemm and Lipps (1976), Sommeria (1976), Moeng (1984), Nieuwstadt and Brost (1984), Sykes and Henn (1988), Schmidt and Schumann (1989), and Mason (1989). Direct simulation of the atmospheric boundary layer were performed by e.g., Krettenauer and Schumann (1992), Coleman et al. (1990). LES and DNS models proved to be an attractive source of turbulent data, especially because of known difficulties with assembling suitable data bases on atmospheric turbulence.

One of the basic features of atmospheric boundary layer convection is the exchange of mass, momentum and heat between the top of the mixed layer and the stably stratified layer above. The exchange is triggered by thermals penetrating the stable layer and forcing entrainment of warmer air into the mixed layer (Deardorff et al., 1980). Effects of entrainment are important to the structure of the mixed layer and have been studied experimentally (e.g. Caughey and Palmer, 1979; Young, 1988) and also numerically (e.g., Deardorff, 1974). Based on these studies, numerous parametrization schemes been presented (e.g. Lilly, 1968; Zeman and Tennekes, 1977; Mahrt, 1979; Boers, 1989).

An interesting aspect of convection was reported by Adrian et al. (1986) during their non-penetrative (without entrainment) convection experiments in a tank. The tank, 1.45 m x 1.5 m x 0.2 m in size, was heated from below by electrical mats and had an insulated solid lid at the top. The results obtained showed an intriguing resemblance of various turbulence statistics in the lower portion of the non-penetrative mixed layer and in penetrative atmospheric boundary layer. Non-penetrative convection in a tank was successfully simulated by Krettenauer and Schumann (1992) by using LES and DNS models. Krettenauer and Schumann demonstrated that numerical results can be taken to be as reliable as laboratory measurements.

The goal of this study is also to simulate numerically the non-penetrative dry boundary layer using a LES model. Nevertheless, the focus of this paper is different. We intend to compare the obtained results for non-penetrative convection with the numerical simulation of the penetrative convection in the atmosphere. With such a comparison, we aim to study the fundamental factor which distinguishes both cases, i.e. the entrainment on the top of the convective atmospheric boundary layer.

2. MODEL DESCRIPTION

2.1. Basic equations

The LES model applied in this study is based on a system of the differential equations consisting of conservation laws for momentum, mass and the first law of thermodynamics (e.g. Deardorff, 1973, a, b, Lilly, 1987, Nieuwstadt, 1990):

$$\frac{\partial \overline{u_i}}{\partial t} + \frac{\partial \overline{u_i}\,\overline{u_j}}{\partial x_j} = -\frac{\partial \pi}{\partial x_j} + \beta\,(\overline{\theta} - \theta_o)\,\delta_{ij} - 2\varepsilon_{ijk}\,\Omega_j\,\overline{u_k} - \frac{\partial \tau_{ij}}{\partial x_j}$$

$$\frac{\partial \overline{\theta}}{\partial t} + \frac{\partial \overline{u_j}\,\overline{\theta}}{\partial x_j} = -\frac{\partial H_j}{\partial x_j} \qquad (1)$$

$$\frac{\partial \overline{q}}{\partial t} + \frac{\partial \overline{u_j}\,\overline{q}}{\partial x_j} = -\frac{\partial Q_j}{\partial x_j}$$

$$\frac{\partial \overline{u_j}}{\partial x_j} = 0$$

where x_j are the Cartesian coordinates (i = 1, 2, 3), x_3 is parallel to gravity acceleration, $\overline{u_i}$ are the components of the velocity vector, $\overline{\theta}$ and $\overline{q}$ are the perturbations of the virtual potential temperature and specific humidity with respect to the reference state values which are chosen to be constant with height, $\pi = \overline{P} + \frac{2}{3} E$ is the air pressure perturbation modified by adding a term proportional to the subgrid turbulent kinetic energy $E = \frac{1}{2}(\overline{u_k u_k} - \overline{u_k}\,\overline{u_k})$, $\overline{P} = \frac{\overline{p} - p_o}{\rho_o}$ is the pressure perturbation term, $\tau_{ij} = (\overline{u_i u_j} - \overline{u_i}\,\overline{u_j}) - \frac{2}{3} E \delta_{ij}$ is the stress tensor (note that $\tau_{kk} = 0$), $H_j = (\overline{u_j \theta} - \overline{u_j}\,\overline{\theta})$ is the subgrid turbulent temperature flux, $Q_j = (\overline{u_j q} - \overline{u_j}\,\overline{q})$ is the subgrid turbulent humidity flux, $\beta = g/\theta_o$ is the buoyancy parameter, Ω_j is the component of Earth's angular velocity, δ_{ij} is Kronecker's delta, and ε_{ijk} is the unity tensor, θ_o, p_o are the reference state potential temperature and pressure. The overbar indicates a running grid volume average:

$$\overline{f}(x, y, z) = \frac{1}{\Delta x \Delta y \Delta z} \int_{x-\Delta x}^{x+\Delta x} \int_{y-\Delta y}^{y+\Delta y} \int_{z-\Delta z}^{z+\Delta z} f(X, Y, Z)\, dX\, dY\, dZ \qquad (2)$$

where Δx, Δy, Δz are the grid increments. It can be proved that $\overline{\overline{f}} \neq \overline{f}$ and that the averaging operator commutes: $\frac{\partial \overline{f}}{\partial x_k} = \overline{\frac{\partial f}{\partial x_k}}$. The use of potential temperature in non-divergent system is approximate, although admittedly common (Lilly, 1995).

2.2. Subgrid model

The set (1) of grid volume averaged equations constitutes a system of six differential equa-

tions with six unknown quantities: $\overline{u_1}$, $\overline{u_2}$, $\overline{u_3}$, $\overline{\theta}$, $\overline{q}$, and π. The system (1) also contains three "subgrid" terms τ_{ij}, H_j, Q_j, which have to be related to the grid volume averaged variables. The subgrid fluxes are parametrized as follows (e.g., Deardorff 1973 a, b):

$$\begin{aligned} \tau_{ij} &= - k_m \left(\frac{\partial \overline{u_i}}{\partial x_j} + \frac{\partial \overline{u_j}}{\partial x_i}\right) \\ H_j &= - k_h \frac{\partial \overline{\theta}}{\partial x_j} \\ Q_j &= - k_q \frac{\partial \overline{q}}{\partial x_j} \end{aligned} \qquad (3)$$

where k_m is the eddy viscosity, and k_h and k_q are the eddy diffusivities.The eddy viscosity and diffusivity coefficients are assumed to be functions of the subgrid turbulent kinetic energy E, mixing length λ, and the Prandtl number Pr:

$$\begin{aligned} k_m &= c_m \ \lambda \, E^{1/2} \\ k_h &= k_q = k_m / Pr. \end{aligned} \qquad (4)$$

The subgrid turbulent kinetic energy E satisfies the following prognostic equation which can be derived based on the set (1) (e.g., Lilly, 1987):

$$\frac{\partial E}{\partial t} + \frac{\partial \overline{u_j} E}{\partial x_j} = - \tau_{ij} \frac{\partial \overline{u_i}}{\partial x_j} + \beta \, H_3 - \frac{\partial}{\partial x_j} (T_j + P_j) - \varepsilon \qquad (5)$$

where ε is the viscous dissipation rate, T_j is the turbulent transport term, and $P_j = (\overline{\pi \, u_j} - \overline{\pi} \, \overline{u_j})$ is the pressure term. The first and the last terms on the right hand side are expected to be dominant during free convection.

The turbulent transport, pressure, and dissipation terms in (5) can be parametrized in the following way (e.g., Deardorff 1973 a, b):

$$P_j + T_j = - c_e k_m \frac{\partial E}{\partial x_j} \tag{6}$$

$$\varepsilon = c_\varepsilon \frac{E^{3/2}}{\lambda} \tag{7}$$

where c_e and c_ε are constants, λ is the mixed length. The mixing length was defined as (Schumann, 1991 a):

$$\lambda = \min (\Delta, c_L z) \tag{8}$$

where the parameter $\Delta = (\Delta x+\Delta y+\Delta z)/3$ must fall within the inertial subrange. The following numerical values of constants were adopted: $c_\varepsilon = 0.845$, $c_e = 2.0$, $c_m = 0.0856$, $c_h = 0.204$, $c_L = 0.845$ (Schumann, 1991 a).

Following Schumann (1991 a) it was assumed that $Pr = k_m/k_h = c_m/c_h$. In stably stratified parts of the flow, the vertical subgrid heat and scalar fluxes were modified by assuming that $Pr = \frac{c_m}{c_h}(1 + 0.3\,\Delta^2 \frac{N^2}{E})$, where $N = (\beta\, \partial\overline{\theta}/dz)^{0.5}$ is the Brunt-Väisälä frequency. The modification reduces the values of eddy diffusivities: $k_h = k_m / Pr = c_h\, \lambda\, E^{3/2} / (E + 0.3\, \Delta^2 N^2)$. The reduction can be explained by the fact that in stable conditions all vertical motions including diffusion are opposed by buoyancy. For very stable stratification, $\Delta^2 N^2 >> E$, and $k_h \rightarrow c_h\, E^{3/2} / (0.3\, \Delta\, N^2)$, which agrees with results obtained previously by Lilly et al. (1974) and Weinstock (1978).

The constants c_m and c_ε can be related to the Smagorinsky constant c_s as $c_s = c_m^{3/4} / c_\varepsilon^{1/4}$ (e.g., Sullivan et al., 1994). For the constants listed above one can obtain $c_s = 0.163$. The length scale Δ is assumed to be equal to the average of the grid distances (Δ = 73.3 m, for values in Table 1) rather than root-mean-cube ($\Delta' = [\Delta x \Delta y \Delta z]^{1/3}$ = 58.2 m), as assumed by Deardorff (1974). Deardorff's form has been recently shown to be correct by Scotti et al. (1993). For grid anisotropy, Scotti et al. (1993) proposed correction of constants in eddy diffusivity coefficients. For

the aspect ratio $\Delta z/\Delta x = 1/5$ (Table 1), c_S is recommended to be multiplied by 1.3. It can be noted, however, that because the ratio of both length scales Δ and Δ' is also about 1.3, the recommended decrease of the length scale and the increase of c_S cancel each other and consequently any correction is necessary.

2.3. Boundary conditions and numerical scheme

Horizontal boundary conditions were assumed to be periodic. At the lower boundary, constant (in time and space) surface temperature and humidity fluxes were assumed, $H_O = 0.001$ K m/s, and $Q_O = 0.005$ g/kg m/s. The vertical derivative of the turbulent kinetic energy was assumed to be zero. The Monin-Obukhov similarity formulation was employed to calculate momentum fluxes (e.g. Schmidt and Schumann, 1989). The upper boundary conditions were assumed to be stress free for horizontal velocity components, and zero for vertical velocity. Moreover, a specified lapse rate Γ for temperature (0 K/km or 3 K/km), zero lapse rate for humidity, and zero turbulent kinetic energy were assumed at the top of the domain.

The numerical algorithm of the model was developed by Deardorff (1973 a, b). Adams-Bashforth's scheme was employed for integration in time. Adams-Bashforth's scheme is known to be unconditionally unstable, nevertheless, because the instability is weak and because of stabilizing effects of the viscous terms, the method can be successfully used in practice. Central finite differences were used to approximate space derivatives on Arakawa's staggered mesh C with uniform spacing. All scalar quantities were located in the center of a grid volume. The Poisson equation for pressure was obtained by imposing zero finite-differences divergence operator upon the finite-differences analog of the momentum equations in (1). The obtained equation was solved by "fast Fourier transform" in horizontal, and "3-diagonal algorithm" in vertical. A numerical “sponge” was applied in the upper portion of the model (the top ten grid points) to reduce reflection of gravity waves (Nieuwstadt et al., 1992).

Initially, the atmosphere was assumed to be at rest. The initial potential temperature profile was constant (=300 K) with height within the mixed layer. Above the mixed layer, the temperature increased with a constant positive lapse rate Γ. Initial random perturbations were imposed upon the temperature field within the mixed layer (e.g., Nieuwstadt et al., 1992). The initial potential humidity profile was constant (=1g/kg) with height within the mixed layer and zero above. The geostrophic wind and the Coriolis terms were assumed to be zero. The roughness length was z_o = 0.16 m.

2.4. Characteristics of performed simulations

The parameters characterizing the simulations performed are presented in Table 1. In the table, a symbol N refers to the non-penetrative simulation, and P to the penetrative simulation. Symbols Δt, Δx, Δy, and Δz indicate time and space increments, $w* = (\beta z_i H_o)^{1/3}$, $T* = H_o/w*$, and $q* = Q_o/w*$ are the convective scales for vertical velocity, temperature, and humidity respectively, z_i is the mixed layer height (defined as the height where the temperature heat flux has the minimum value), and L is the Monin-Obukhov length, $t^* = z_i/w*$ is the convective time scale.

Runs N and P differ in the temperature lapse rate Γ at the top of the computational domain. The temperature lapse rate Γ was 3 K/km for run P. In run N the upper boundary was insulated (Γ=0) and moisture impermeable. In order to minimize effects of the upper boundary, the computational domain during run P extends to 2 z_i = 1100 m . The computational domain during run N is z_i = 600 m. The sponge coefficient in run P was 0.01 s^{-1}. The numerical "sponge" was turned off during the N simulation.

Table 1. Characteristics of performed simulations

Run	Time steps	Space domain	Δt [s]	$\Delta x=\Delta y$ [m]	Δz [m]	$w*$ [m/s]	$T*$ [K]	$q*$ [g/kg]	z_i [m]	$-z_i/L$	$t*$ [s]

N	6000	32x32x30	2.5	100	20	0.267	0.0037	0.019	600	120.0	37.5
P	6000	32x32x55	2.5	100	20	0.262	0.0038	0.019	550	161.2	35.0

Krettenauer and Schumann (1992) used 64 x 64 x 16 grid points in their simulation of non-penetrative convection. Their model was run for a time interval of t = 35 t_*, and averaged the results within a period of 5 t_*. As can be seen in Table 1, run N uses 32 x 32 x 30 grid points, while there are 32 x 32 x 55 grid points in run P. Consequently, runs N and P use less grid points in the horizontal and a larger amount of grid points in the vertical with respect to Krettenauer and Schumann's (1992) simulation. It should be mentioned that Schumann (1991), Nieuwstadt et al.(1992) have shown that basic characteristics of turbulence can be accurately represented even by a low number of grid points

Calculations were performed in a horizontal domain size of 5.5 z_i for run N, and 5.8 z_i for run P. A domain of size 4 z_i is considered by Krettenauer and Schumann (1992) to be sufficient and also minimum to cover all important scales. Sykes and Henn (1988) investigated the impact of increasing numerical resolution and increasing domain size. They found that differences between the runs with different domain sizes are small.

The time integration during run N was performed over a period of 6.7 t*, with $t_* \approx 37.5$ minutes. The time integration during run P was performed over a period of 7.1 t_*, with $t_* \approx 35$ minutes. Figure 1 indicates that the kinetic energy in run N becomes approximately steady after about 5000 time steps, which is 5.6 t_*. A similar plot (not shown) was also obtained for run P. Figure 1 shows that the subgrid portion of the turbulent kinetic energy in N simulation (as well as in run P) amounts to about 30% of the total kinetic energy. Therefore, 70% of turbulent kinetic energy is directly resolved in this calculation. Consequently, the simulations performed can be classified as LES. For comparison, in the simulation of Krettenauer and Schumann (1992) about 80% of turbulent kinetic energy was directly resolved.

The results of all simulations were averaged in time and also horizontally in space. The time averaging was executed during the last 500 time steps, every 50 time steps during run N, and every

25 time steps during run P. Large values of the parameter $-z_i/L$ in Table 1 during both simulations indicate extremely convective conditions, even though w_* and z_i are relatively small.

3. THE RESULTS

3.1. General description of thermal convection

The vertical profiles of the total and subgrid virtual potential temperature fluxes are shown in Figure 2. The total fluxes are defined as $H = \langle w' \theta' \rangle + sgc$, where $\langle\ \rangle$ indicates an averaged quantity (over time and horizontally in space), the primed quantities are defined as departures from horizontal means. The subgrid component of the total flux is defined as: $sgc = \langle H3 \rangle$, where $H3$ is described by eq. (3). Figure 2 indicates that both total fluxes are linear within the mixed layer. As expected, the temperature flux at the top of the mixed layer vanishes in run N, while for run P the flux at the top of the mixed layer is negative and equal to about 25% of its surface value. The temperature flux in the penetrative case vanishes at $z = 1.2\, z_i$. The subgrid portion of the flux increases at the top of the penetrative mixed layer, nevertheless, it remains much smaller than the total flux.

Figure 3 shows the conditionally averaged dimensionless potential temperature excess (i.e., $\langle \theta' \rangle = \langle \theta^{\Uparrow} - \{\theta\} \rangle$, $\theta^{\Uparrow}$ is the temperature in updrafts, and $\{\}$ denotes horizontal averaging) and vertical velocity (i.e., $\langle w' \rangle = \langle w^{\Uparrow} \rangle$, since $\{w\} = 0$) in updrafts during runs N and P. Updrafts were identified by positive vertical velocities, $w^{\Uparrow} > 0$. It is interesting to see that the dimensionless vertical velocity in updrafts during the penetrative convection is nearly the same as in the non-penetrative case. The temperature excesses in updrafts in runs N and P coincide up to approximately $0.5\, z_i$. Above this level, updrafts in run P are relatively cooler, due to heating of the upper portion of the mixed layer by entraining warm air from the capping stable layer.

The dimensionless mean temperature excess and vertical velocity in downdrafts (identified by negative vertical velocities) in both simulations are presented in Figure 4. Temperature excesses

in downdrafts in runs P and N coincide only below 0.2 z_i. Above, downdrafts in run P are relatively warmer as they carry entrained warm air from the capping stable layer. The vertical velocities in downdrafts during both simulations are the same up to approximately 0.4 z_i. Above this level, the vertical velocity of downdrafts during run P is slightly smaller. This is caused by the fact that downdrafts in run P are positively buoyant. In contrast, in the non-penetrative case, downdrafts are negatively buoyant and sink relatively faster. The shape of the vertical velocity profiles and temperature profiles in updrafts and downdrafts is nearly symmetric. The magnitude of vertical velocity in updrafts is slightly larger than in downdrafts, which agrees with atmospheric observations of Young (1988).

The temperature flux vanishes at the top of the non-penetrative domain due to vanishing of the vertical velocity at the boundary. During penetrative convection, the vertical velocity in updrafts at the top of the mixed layer is small but positive and the temperature excess is relatively large and negative (Figure 3). Consequently, on average, updrafts at the top of the penetrative mixed layer contribute to the negative temperature flux. On the other hand, the vertical velocity in downdrafts near the top of the mixed layer is small and negative while the temperature excess is relatively large and positive (Figure 4). Thus, downdrafts at the top of the penetrative mixed layer also contribute on average to the negative temperature flux. The resulting total temperature flux is negative near the top of the mixed layer during penetrative convection. A similar conclusion was obtained by Schumann and Moeng (1991).

Figure 5 shows that in the bulk of the mixed layer, the relative area covered by updrafts during run N is approximately constant with height. This agrees with the result of Moeng and Rotunno (1990). The figure indicates that updrafts cover $A^{\Uparrow} = 43\%$, while the relative area covered by downdrafts is $A^{\Downarrow} = 57\%$. It can be noticed, that since the horizontally averaged vertical velocity must vanish (mass continuity restraint), then

$$A^{\Uparrow} \langle w^{\Uparrow} \rangle + A^{\Downarrow} \langle w^{\Downarrow} \rangle = 0 \qquad (9)$$

Substituting values of $A^{\Uparrow}$ and $A^{\Downarrow}$, yields $\langle w^{\Uparrow} \rangle = -1.3 \langle w^{\Downarrow} \rangle$. For $\langle w^{\Downarrow} \rangle = -0.5\, w_*$ (see Figure 4), we obtain that $\langle w^{\Uparrow} \rangle = 0.65\, w_*$, which agrees with Figure 3. Consequently, non-penetrative

convection is composed of narrower updrafts with larger velocities and wider and slower downdrafts. A similar process is also observed in penetrative convection.

The relative area covered by updrafts in run P has a minimum near the top of the mixed layer. A similar conclusion was obtained by Moeng and Rotunno (1990) based on Moeng's LES model (1984). The minimum value of $A^{\Uparrow}$ produced by Moeng's model is about 40% (e.g. Schumann and Moeng, 1991). It can be noticed in Figure 5 that $A^{\Uparrow}$ is about 25% in run P. A comparison of various LES codes performed by Nieuwstadt et al. (1990) confirms that Schumann's subgrid parameterization, described in Section 2.2, yields relatively small values of $A^{\Uparrow}$.

In Figure 6, the vertical cross-sections of an instantaneous vertical velocity field is depicted for non-penetrative convection. The figure shows that non-penetrative convection is organized into separate columns of updrafts and downdrafts extending from the bottom to the top of the domain. A similar result was also obtained by Moeng and Rotunno (1990). Moeng and Rotunno observed that updrafts line up as irregular polygons in the lower levels and are more isolated above. Updrafts that originate at the intersections of these polygons are more likely to survive to the upper levels.

During penetrative convection area covered by updrafts decreases with height. According to Schmidt and Schumann (1989) large thermals have higher thermal velocity and suck in smaller thermals from their neighborhood. Since updrafts in penetrative convection are negatively and downdrafts are positively buoyant, work has to be performed against buoyancy to support vertical motions of air near the top of the mixed layer and above it. The magnitude of the work performed W (for a unit of mass over a unit of time) is proportional to the negative area in Figure 2. The negative area is located between the curve representing the flux and the z-axis, from the level h_o at which the heat flux crosses zero to the level $h \approx 1.2 z_i$, where the heat flux vanishes. The buoyant production of turbulent kinetic energy (for a unit of mass over a unit of time) is proportional to the positive area in the same figure, from the surface to the level h_o. Both quantities W and P can be estimated as follows:

$$W = \int_{h_o}^{h} \beta H \, dz = 0.5 \, \frac{w_*^3}{1 - R} \, (1.2 \, R^2 - 0.2 \, R) \tag{10}$$

$$P = \int_0^{h_o} \beta\, H\, dz = 0.5\, \frac{w_*^3}{1 - R}$$

where R is the heat flux ratio $R = H_i / H_o$, $h_o = z_i /(1 - R)$ is the height at which the heat flux crosses zero (Sorbjan, 1995). In (10), the temperature flux was assumed to be linear and equal to $H = H_o(1-z/z_i)$ for non-penetrative convection. In the case of penetrative convection, two linear profiles were used: $H = H_o [(1 - z/z_i) + R\, z/z_i]$ for $z \le z_i$, and $H = 5\, R\, H_o\, (1.2 - z/z_i)$ for $z_i < z \le 1.1\, z_i$.

If we compare areas of positive and negative regions of the heat flux, it can be seen that $W = (1.2R^2 - 0.2\, R)\, P$. This suggest that for R = - 0.2 about $(1.2R^2 - 0.2\, R) \approx 9\%$ of the turbulent kinetic energy generated by surface heating goes to support entrainment. Some other previously presented estimates range from 4% to 20% and were discussed by Lilly (1989).

Analysis of Figures 2-6 brings the following picture of the non-penetrative convection. Rising fluid is initially accelerated by buoyancy. The acceleration decreases with height because thermals lose their buoyancy through a heat transfer to the surrounding fluid. Deceleration occurs when updrafts approach the upper boundary. At the top, a rigid lid forces the fluid to spread. After this horizontal spreading, temperature of air that was formerly in thermals becomes lower than the mean temperature of the mixed layer (which is steadily warming). Consequently, the ascending thermals are converted into a cool, descending flow. The full cycle consisting of a rising and a sinking phase lasts approximately: $z_i/(0.5w_*) + z_i/(0.65w_*) = 3.5\, t_*$, where the vertical velocities were estimated based on Figures 3 and 4.

In the case of penetrative convection, rising fluid is also initially accelerated by buoyancy. The acceleration decreases with height. Deceleration occurs when updrafts encounter a descending positively buoyant flow, or enter the entrainment zone. Updrafts, which are in average negatively buoyant, are still able to penetrate the stable layer. The penetration forces entrainment of warm air into the mixed layer. Downdrafts are in average positively buoyant. They gradually lose their buoyancy through a heat transfer to the surrounding fluid.

In Figure 7, the dimensionless components of the resolvable turbulent kinetic energy budget are depicted for both runs N and P. In the figure, DD = $< \varepsilon >$ is the the averaged dissipation term calculated based on equation (7), BP = $\beta <w'\theta'>$ is the buoyant production term, TT = 0.5 d/dz

$\langle u'^2w'+v'^2w'+w'^3\rangle$ is the turbulent transport term, PP = d/dz $\langle w'P'\rangle$ is the pressure transport term and SP = $-(\langle u'w'\rangle d\langle\bar{u}\rangle/dz + \langle v'w'\rangle d\langle\bar{v}\rangle/dz)$ is the shear production. Generally, the turbulent kinetic energy is generated by buoyancy BP and lost due to the viscous dissipation DD. The turbulent transport redistributes energy from near the lower surface (negative values of TT) to the top (positive values of TT). The pressure transport term PP has a tendency to oppose this transfer. The strongest differences between penetrative and non-penetrative cases are reflected upon the largest components of the energy balance, i.e. in dissipation DD and in buoyancy production BP.

For steady state, non-penetrative convection, the mixed layer averaged value of the dissipation ε_N should be exactly equal to the mean buoyancy production, i.e. :

$$\varepsilon_N = \frac{1}{z_i}\int_0^{z_i} H_o\,(1-z/z_i)\,dz = 0.5\; w_*^3 / z_i \qquad (11)$$

Similarly, for a steady state of penetrative convection:

$$\varepsilon_P = 0.5\,\frac{(1+R)w_*^3}{(1-R)\;z_i} \qquad (12)$$

Consequently,

$$\varepsilon_P / \varepsilon_N = (1 + R) / (1 - R) \qquad (13)$$

This suggest that dissipation in penetrative convection equals about (1 + R) / (1 - R) = 67% of the dissipation generated in the non-penetrative case (for R = - 0.2). This agrees with values in Figure 7.

3.2. Temperature fields

Dimensionless profiles of the potential temperature lapse rate during runs N and P are shown in Figure 8. Both profiles coincide up to the level $z/z_i = 0.5$. Above $z/z_i = 0.6$, the profile for run N is positive which indicates the counter-gradient transport of heat in this region. The counter-

gradient transport of heat for run P takes place in a layer $0.5 < z/z_i < 0.75$, where both the lapse rate and the flux are positive.

Figure 9 shows profiles of the dimensionless total and subgrid temperature variance during runs N and P. The total temperature variance is defined as $\sigma_\theta^2 = \langle\theta'^2\rangle + sgc$, where the subgrid component of the total variance is defined as: $sgc = 5 \langle H_3\rangle^2 / \langle E\rangle$, $\langle H_3\rangle$ is the averaged subgrid vertical temperature flux, and $\langle E\rangle$ is the averaged subgrid turbulent kinetic energy (Nieuwstadt et al., 1992).

Both total variances in Figure 9 are in agreement up to the level $z/z_i = 0.8$. Near the top of the mixed layer, the dimensionless variance for penetrative convection exhibits a rapid increase of its values. This fact can be explained by using an approximate expression which can be obtained from the simplified temperature variance equation, with only production and dissipation terms retained (Sorbjan, 1989):

$$\frac{\langle\theta'^2\rangle}{\tau} \approx - \langle w'\,\theta'\rangle \frac{\partial\langle\overline{\Theta}\rangle}{\partial z} \qquad (14)$$

where τ is the time scale. Since the temperature flux is negative at the top of the mixed layer, the above equation indicates that the temperature variance will increase if the temperature lapse rate increases.

Dimensionless third moment of temperature during runs N and P is shown in Figure 10. The penetrative curve agrees with results obtained by Kumar et al. (1986) in a tank. Both curves approximately coincide up to $z/z_i = 0.9$. Only the resolvable portion of the moment is shown in Figure 10. Consequently, the values of the moment near the surface are not reliable.

3.3. Humidity fields

Figure 11 depicts the dimensionless total specific humidity fluxes during runs N and P. The total fluxes are defined as $Q = \langle w'q'\rangle + sgc$, where sgc denotes the subgrid component of the total flux defined as: $sgc = \langle Q_3 \rangle$. The total flux in run N is not exactly linear. This indicates that

the simulation time in this run was too short to achieve the steady state. The magnitude of the humidity flux at the top of the mixed layer is about 20% of the surface value in run P.

Dimensionless humidity lapse rates during runs N and P are shown in Figure 12. In the figure, both profiles approximately coincide up to the level $z/z_i = 0.4$. Above $z/z_i = 0.6$, the non-penetrative lapse rate is positive which indicates the counter-gradient transport of moisture in the upper portion of the mixed layer. In the penetrative case, the humidity flux in Figure 11 is positive while the humidity lapse rate in Figure 12 is negative. Interestingly, this implies that the counter - gradient transport of humidity is not present in the penetrative case. A positive humidity lapse rate near the top of the non-penetrative boundary layer denotes an accumulation of mass near the upper surface. The humidity lapse rate at the top in the penetrative case is negative and indicates drying by entrained air.

Wyngaard (1984), Moeng and Wyngaard (1984) decomposed scalar fields C into "bottom-up" and "top-down" components, C_b and C_t. The "bottom-up" component was assumed to be driven by the surface flux, while the "top-down" component was due to entrainment. For mean humidity fields, two similarity functions g_b and g_t were defined as:

$$\frac{z_i}{c_*}\frac{\partial C_b}{\partial z} = - \; g_b(z/z_i)$$

$$\frac{z_i}{c_*}\frac{\partial C_t}{\partial z} = - \; R_c \, g_t(z/z_i) \qquad (15)$$

where R_c is the scalar flux ratio at the top and the bottom of the mixed layer, c_* is the convective scale defined analogously to T_* and q_*.

In non-penetrative case, we have $R = R_c = 0$. Consequently, the "bottom-up" function q_b is identical with the dimensionless humidity lapse rate in our non-penetrative run shown in Figure 12. The difference of the dimensionless lapse rates in penetrative and non-penetrative cases in Figure 12 defines the "top-down" function g_t. A similar approach was adopted by Sorbjan (1989) who proposed to decompose dimensionless statistics of turbulence during penetrative convection into non-penetrative and residual components. Consequently, his decomposition and Wyngaard's

(1984) “bottom-up” and “top-down” decomposition are equivalent in the considered case.

Moeng and Wyngaard (1984) assumed that the “bottom-up” and “top-down” de-composition applies to humidity and temperature fields alike. Validity of this assumption can be verified by comparing Figures 8 and 12. The comparison shows that the dimensionless temperature and humidity lapse rates for non-penetrative convection are equal:

$$\frac{z_i}{q_*}\frac{\partial q}{\partial z} = \frac{z_i}{T_*}\frac{\partial \Theta}{\partial z}. \qquad (16)$$

Dimensionless total humidity variances during runs N and P are shown in Figure 13. The total humidity variance is defined as $\sigma_q^2 = {<q'^2>} + sgc$, where the subgrid component of the total variance is defined as: $sgc = 5 <Q3>^2/<E>$, $< Q3>$ is the averaged subgrid vertical humidity flux, and $<E>$ is the averaged subgrid turbulent kinetic energy.

Inspection of Figures 9 and 13 indicates that dimensionless total variances for temperature and humidity are approximately equal in the non-penetrative case. This fact can also be confirmed in Figure 14 which shows that temperature and humidity during non-penetrative convection are perfectly correlated (with numerical accuracy). This is a consequence of the fact that both scalars follow the some governing equations and have analogous boundary conditions. During penetrative convection, $r_{\theta q}$ is less than unity and varies from about 0.9 near the surface to about -0.7 at the top of the mixed layer.

The correlation coefficient $r_{\theta q}$ in the surface layer was reported to be less than unity by many investigators. For instance, Wyngaard et al. (1978) after analysis of data collected in convective conditions over the East China Sea concluded that $r_{\theta q} \approx 0.8$. During convective conditions over land, Druilhet et al. (1983) obtained $r_{\theta q} \approx 0.6$. Guillement et al. (1983), form a series of measure-

ments in convective conditions over land, evaluated that $r_{\theta q} = 0.54$ in the inertial subrange. Sorbjan (1991) found that in convective conditions $r_{\theta q} = 0.76$. Deardorff (1974) in his large eddy simulation of the Wangara data obtained the correlation coefficient $r_{\theta q}$ (between resolvable quantities) to be about 0.6 near the surface. Our results imply that the lack of perfect correlation during penetrative convection is caused by the drying effects of entrainment.

3.4. Velocity fields

Dimensionless total horizontal and vertical velocity variances σ_u^2, σ_v^2, σ_w^2, during runs N and P are shown in Figure 15. Each of the total velocity variances consists of resolvable and subgrid terms. For instance, $\sigma_u^2 = \langle u'^2 \rangle + sgc$, where the subgrid component $sgc = \frac{2}{3} \langle E \rangle$, and $\langle E \rangle$ is the averaged subgrid turbulent kinetic energy. The curves obtained in run N are in accord with results of Krettenauer and Schumann (1992) while the curves simulated in run P coincide with results presented by Nieuwstadt et al. (1992).

Values of the dimensionless variances in non-penetrative case are larger than in the penetrative one. This fact is related to the reduction of the dissipation rate described by Equation. 13. Assuming in this equation that the dissipation is related to the total turbulent kinetic energy $E_t = \langle u'_k{}^2 \rangle/2 + \langle E \rangle$ as: $\varepsilon \sim E_t^{3/2} / z_i$, we obtain that the ratio for both runs, $E_t^P / E_t^N = [(1 + R) / (1 - R)]^{2/3}$. For R = - 0.2, we estimate that $E_t^P / E_t^N \sim 0.76$. Consequently, the total turbulent kinetic energy during penetrative convection is reduced by about 24% with respect to the non-penetrative case. The reduction is due to mixing of the entrained air with the mixed layer air. Assuming the same reduction for each of the velocity variances, we obtain that velocity variances should be reduced in about $\frac{2}{3} * 24\% = 16\%$. It can be examined by inspection that this estimate agrees with Figure 15.

Near the top of the mixed layer in Figure 15, values of the dimensionless horizontal variances in non-penetrative case are larger than near the lower surface. This effect can be related to the fact

that lower boundary conditions assume presence of a drag while the boundary condition at the top of the domain is stress-free. Effects of “no-slip” and “free-slip” boundary conditions in non-penetrative convection were considered by Moeng and Rotunno (1990).

4. CONCLUDING REMARKS

A large eddy simulation model was used to compare statistics of turbulence during non-penetrative and penetrative dry convection. The comparison showed that the presence of entrainment significantly alters dynamics of the mixed layer. In the non-penetrative case, convection is organized into separate columns of updrafts and downdrafts extending from the bottom to the top of the domain. In penetrative convection, updrafts are embedded in slowly sinking air and their horizontal area decreases with height.

In penetrative convection, dimensionless vertical velocity in updrafts is almost the same as in the non-penetrative case. In the upper half of the mixed layer, updrafts in the penetrative case are relatively cooler than the ambient air, due to heating of the upper portion of the mixed layer by entraining warm air from the capping stable layer. Downdrafts are initially warmer as they carry the entrained warm air.

The counter-gradient transport of heat and moisture during non-penetrative convection takes place for $z/z_i > 0.6$. For run P, the counter-gradient transport of heat occurs in a layer $0.5 < z/z_i < 0.75$, while the counter-gradient transport of humidity is not present.

During non-penetrative convection, temperature and humidity are perfectly correlated. During penetrative convection, the correlation coefficient is less than unity and varies from about 0.9 near the surface to about -0.7 at the top of the mixed layer. This decorrelation is due to entrainment.

About 9% of the turbulent kinetic energy generated by surface heating goes to support entrainment. Entrainment reduces the dissipation rate to about 70% of the dissipation generated in the non-penetrative case. The turbulent kinetic energy during the penetrative convection is reduced by about 24% with respect to the non-penetrative case. Velocity variances are reduced by about 16%.

Acknowledgements: This research was sponsored by NSF Grant ATM 9217028. The author would like to thank Dr. Douglas Lilly, Dr. Chin-Hoh Moeng, Dr. N. Andrew Crook and Dr. Richard Doviak for their valuable comments.

5. REFERENCES

Adrian, R. J., R. T. D. S. Ferreira, and T. Boberg, 1986: Turbulent thermal convection in wide horizontal fluid layers. *Expts. in Fluids*, **4**, 121-141.

Agee, E. M., 1987: Mesoscale cellular convection over oceans. *Dyn. Atmos.Oceans*, **10**, 317-341.

Boers, R., 1989: A parameterization of the depth of the entrainment zone. *J. Appl. Meteor.*, **28**, 107-111.

Caughey, S.J., and S.G. Palmer, 1979: Some aspects of turbulence structure through the depth of the convective boundary layer. *Quart. J. Roy. Meteor. Soc.*, **105**, 811-827.

Coleman , G. N., J. H. Ferziger, and P.R. Spalart, 1990: A numerical study of the turbulent Ekman layer. *J. Fluid Mech.*, **213**, 313-348.

Deardorff, J. W., G.E. Willis, and D.K. Lilly, 1969: Laboratory investigation of non-steady penetrative convection. *J. Fluid Mech.*, **35**, 7-31.

Deardorff, J. W., 1972: Numerical integration of neutral and unstable planetary boundary layers. *J. Atmos. Sci.*, **29**, 91-115.

Deardorff, J. W., 1973a: Three-dimensional numerical modelling of the planetary boundary layers. *Workshop on Micrometeorology*, D.A. Haugen, Ed., Amer. Meteor. Soc., 271-311.

Deardorff, J. W., 1973b: The use of subgrid transport equations in a three-dimensional model of atmospheric turbulence. *J. Fluids Eng.*, **95**, 429-438.

Deardorff, J. W., 1974: Three-dimensional numerical study of turbulence in an entraining mixed layer. *Bound.-Layer Meteor.*, **7**, 199-226.

Deardorff, J. W., G.E. Willis, and B. H. Stockton, 1980: Laboratory studies of entrainment zone

of a convectively mixed layer. *J. Fluid Mech.*, **100**, 41-64.

Druilhet, A., J. P. Frangi, D. Guadalia, and J. Fontan, 1983: Experimental studies of the turbulence structure parameters of the convective boundary layer. *J. Climate Appl. Meteor.*, **22**, 594-608.

Guillemet, B., and H. Isaka, 1983: Molecular dissipation of turbulent fluctuations in the convective mixed layer. Part I: Height variations of dissipation rates. *Bound.-Layer Meteor.*, **27**, 141-162.

Krettenauer, K., and U. Schumann, 1992: Numerical simulation of turbulent convection over wavy terrain. *J. Fluid Mech.*, **237**, 261-299.

Lilly, D. K., 1968: Models of cloud-capped mixed layers under a strong inversion. *Quart. J. Roy. Meteor. Soc.*, **94**, 292-309.

Lilly, D. K., D.E. Waco, and S. I. Adelfang. 1974: Stratosphere mixing estimated from high-altitude turbulence measurements. *J. Appl. Meteor.*, **13**, 488-493.

Lilly, D. K., 1987: Modes of turbulence in stably stratified environments: part II. *Lecture Notes on Turbulence*, J. R. Herring and J. C. McWilliams, Eds., World Scientific, 171-217.

Lilly, D. K., 1995: A comparison of incomressible, anelastic, and Boussinesq Dynamics. Submitted to *Atmos. Res*.

Kumar, R. and R.J. Adrian, 1986: Higher order moments in the entrainment zone of turbulent penetrative thermal convection. *J. Heat Trans.*, **108**, 323-329.

Mahrt, L., 1979: Penetrative convection at the top of a growing boundary layer. *Quart. J. Roy. Meteor. Soc.*, **105**, 969-985.

Mason, P.J., 1989: Large-eddy simulation of the convective atmospheric boundary layer. *J. Atmos. Sci.*, **46**, 1492-1516.

Mason, P.J., 1994: Large-eddy simulation: A critical review of the technique. *Quart. J. Roy. Meteor. Soc.*, **120**, 1-26.

Moeng, C.-H., 1984: A large-eddy simulation model for the study of planetary boundary-layer turbulence. *J. Atmos. Sci.*, **41**, 2052-3169.

Moeng, C.-H., and J. C. Wyngaard, 1984: Statistics of conservative scalars in the convective boundary layer. *J. Atmos. Sci.*, **41**, 3161-2062.

Moeng, C.-H., and R. Rotunno, 1990: Vertical velocity skewness in the buoyancy-driven bound ary layer. *J. Atmos. Sci.*, **47**, 1149-1162.

Nieuwstadt , F. T. M., and R. A. Brost, 1986: Decay of convective turbulence. *J. Atmos. Sci.*, **43**, 532-546.

Nieuwstadt , F. T. M., 1990: Direct and large-eddy simulation of free convection. *Proc. 9th Intl. Heat Transfer Conf.*, Jerusalem, vol.1, Amer. Soc. Mech. Engr., pp. 37-47.

Nieuwstadt , F. T. M., P.J. Mason, C. H. Moeng, and U. Schumann, 1992: Large-eddy simulation of convective boundary-layer: A comparison of four computer codes. *Turbulent Shear Flows 8*, Durst H. et al., Eds, Springer-Verlag, 343-367.

Schemm, C. E., and F. B. Lipps, 1976: Some results from a simplified three-dimensional numerical model of atmospheric turbulence. *J. Atmos. Sci.*, **33**, 1021-1041.

Schmidt, H., and U. Schumann, 1989: Coherent structure of the convective boundary layer derived from large-eddy simulation. *J. Fluid Mech.*, **200**, 511-562.

Schumann , U. , 1991a: Subgrid Length-scales for large-eddy simulation of stratified turbulence. *Theor. Comput. Fluid Dyn.*, **2**, 279-290.

Schumann, U., 1991b: Simulations and parameterizations of large eddies in convective atmospheric boundary layers.*Workshop on Fine Scale Modelling and the Development of Parameterization Schemes*, European Centre for Medium-Range Weather Forecasts, 21-51.

Schumann , U., and C.-H. Moeng, 1991: Plume fluxes in clear and cloudy convective boundary layers. *J. Atmos. Sci.*, **48**, 1746-1757.

Scotti, A., C. Meneveau, and D. K. Lilly, 1993: Generalized Smagorinsky model for anisotropic grids. *Phys. Fluids* A, **5** (9), 2306-2308.

Sommeria, G., 1976: Three-dimensional simulation of turbulent processes in an undisturbed trade wind boundary layer. *J. Atmos. Sci.*, **33**, 216-241.

Sorbjan, Z., 1989: *Structure of the Atmospheric Boundary Layer*. Prentice-Hall, 317 pp.

Sorbjan, Z., 1991: Evaluation of local similarity functions in the convective boundary layer. *J. Appl. Meteor.*, **30**, 1565-1583.

Sorbjan, Z., 1995: Toward evaluation of heat fluxes in the convective boundary layer. *J. Appl.Meteor.* , **34**, 1092-1098

Sykes R. I., and D.S. Henn, 1988: A large-eddy simulation of turbulent sheared convection. *J. Atmos. Sci.*, **46**, 1106-1118.

Young, G. S., 1988: Turbulence structure of the convective boundary layer. Part II: Phoenix 78 Aircraft observations of thermals and their environment. *J. Atmos. Sci.*, **45**, 727-735.

Weinstock, J., 1978: Vertical diffusion in a stably stratified fluid.*J. Atmos. Sci.*, **35**, 1022-1027.

Willis, G. E., and J. W. Deardorff, 1974: A laboratory model of the unstable planetary boundary layer. *J. Atmos. Sci*., **31**, 1297-1307.

Wyngaard, J.C., W.T. Pennell, D.H. Lenschow, and M.A. LeMone, 1978: The temperature-humidity covariance budget in the convective boundary layer. *J. Atmos. Sci.*, **35**, 47-58.

Wyngaard, J. C., 1984: Toward convective boundary layer parameterization: a scalar transport module.*J. Atmos. Sci.*, **41**, 102-112.

Wyngaard, J. C., 1992: Atmospheric turbulence. *Ann. Rev. Fluid. Mech.*, 24, 205-235.

Zeman, D., and H. Tennekes, 1977: Parameterization of the turbulent energy budget at the top of the daytime atmospheric boundary layer. *J. Atmos. Sci.*, **34**, 111-123.

TABLE 1. Characteristics of performed simulations

Run	Time steps	Space domain	Δt [s]	$\Delta x=\Delta y$ [m]	Δz [m]	w_* [m/s]	T_* [K]	q_* [g/kg]	z_i [m]	$-z_i/L$	t_* [s]
N	6000	32x32x30	2.5	100	20	0.267	0.0037	0.019	600	120.0	37.5
P	6000	32x32x55	2.5	100	20	0.262	0.0038	0.019	550	161.2	35.0

FIGURE CAPTIONS

Figure 1. Time history of the kinetic energy during run N.

Figure 2. Vertical distribution of the dimensionless total (solid line) and subgrid (dotted line) fluxes of the potential virtual temperature for runs N and P.

Figure 3. Dimensionless mean potential virtual temperature excess and vertical velocity in updrafts for runs N and P.

Figure 4. Dimensionless mean excess of potential virtual temperature and vertical velocity in downdrafts for runs N and P.

Figure 5. Relative area covered by updrafts during runs N and P.

Figure 6. (a) Horizontal (x-y), and (b) vertical (x-z) cross-sections of an instantaneous vertical velocity field during non-penetrative convection. The horizontal cross-section is obtained at $z=0.5z_i$, the vertical cross-section is obtained at $y=0.5L$. Contour interval = $0.15w_*$. Regions with positive velocities are shaded.

Figure 7. Dimensionless components of the resolvable kinetic turbulent energy balance during runs N and P. All terms scaled by w_*^3 / z_i.

Figure 8. Dimensionless lapse rate of potential virtual temperature for runs N and P.

Figure 9. Dimensionless total (solid line) and subgrid (dotted line) variances of potential virtual temperature for runs N and P (scaled by T_*^2).

Figure 10. Dimensionless third moment of the potential virtual temperature (resolvable) during runs N and P.

Figure 11. Dimensionless total (solid line) and subgrid (dotted line) fluxes of specific humidity for runs N and P.

Figure 12. Dimensionless lapse rate of specific humidity for runs N and P.

Figure 13. Dimensionless total (solid line) and subgrid (solid line) variances of specific humidity for runs N and P (scaled by q_*^2).

Figure 14. Correlation coefficient between potential virtual temperature and specific humidity for runs N and P.

Figure 15. Dimensionless total variances of horizontal and vertical components of velocity during runs N and P. All terms scaled by w_*^2.

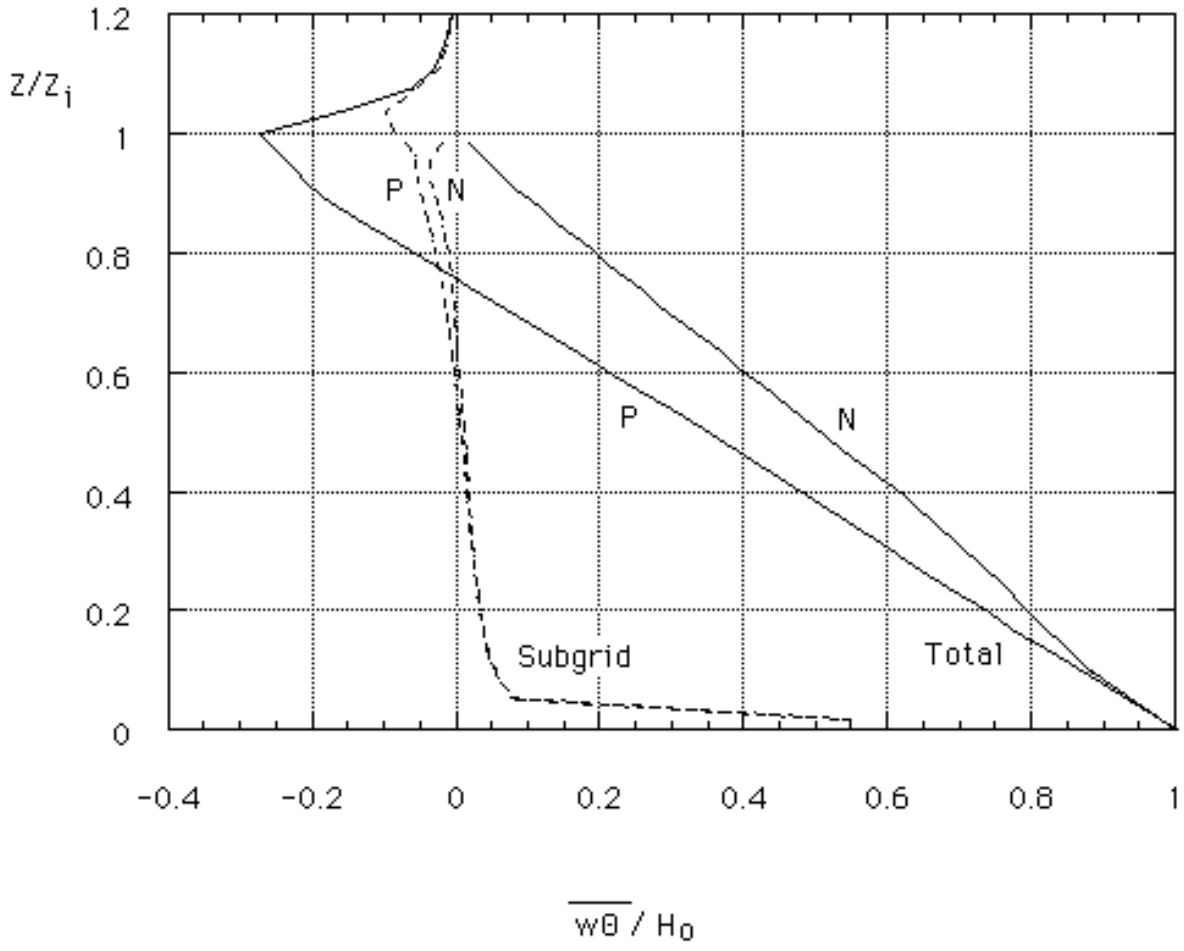

Fig 2

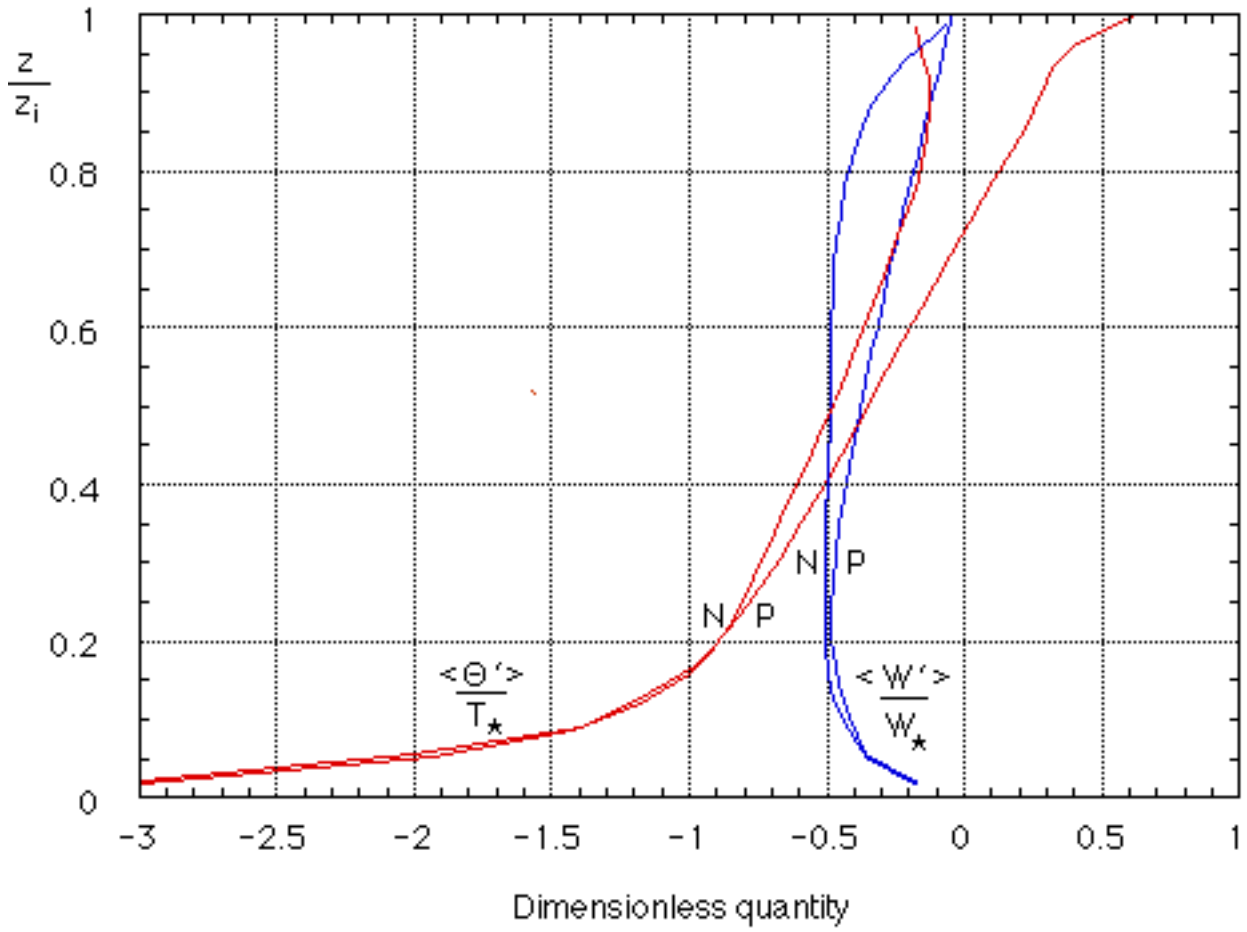
z / z_i
1
0.8
0.6
0.4
0.2
0
-3
-2.5
-2
-1.5
-1
-0.5
0
0.5
1
Dimensionless quantity
<Θ'> / T*
<W'> / W*
N
P
N
P

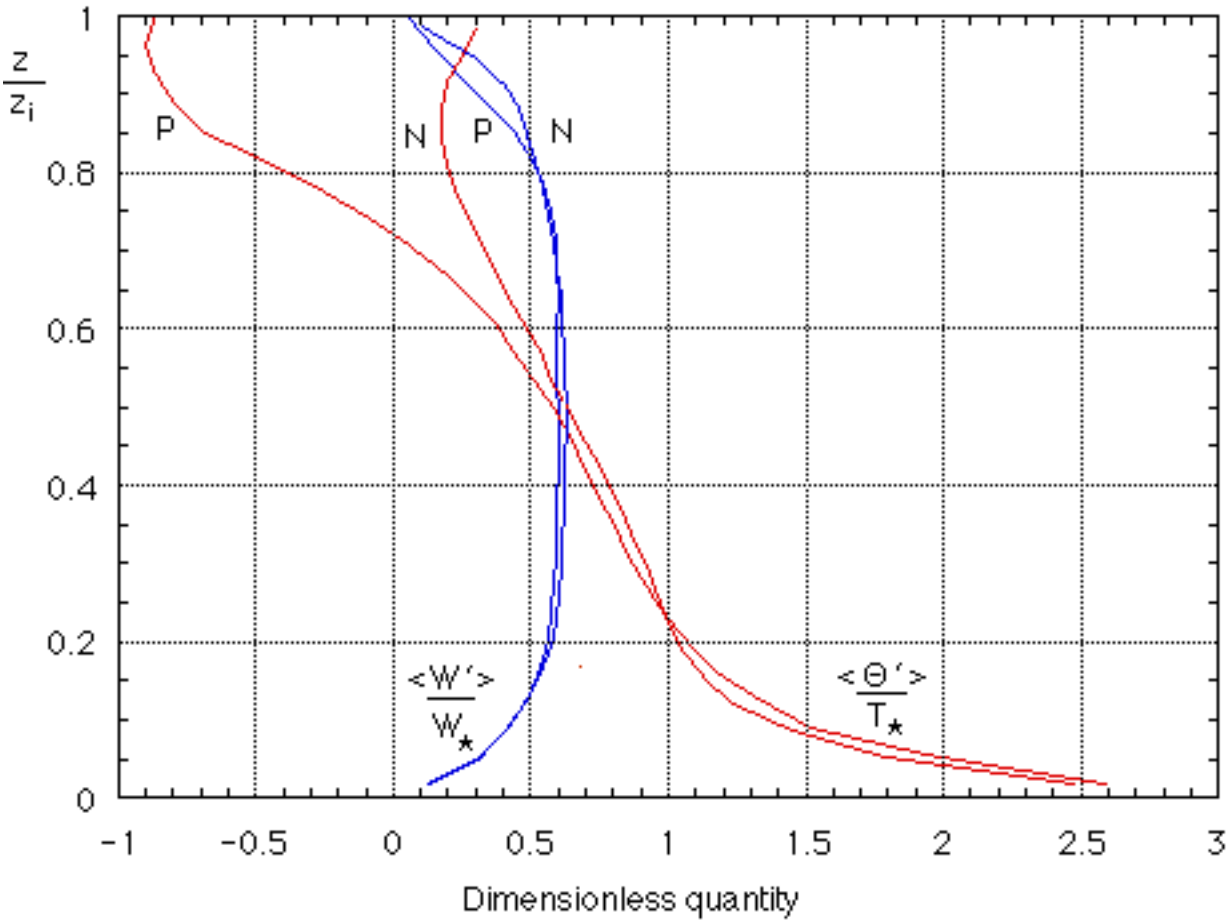
z/z_i
1
0.8
0.6
0.4
0.2
0
P
N
P
N
<W'>/W*
<Θ'>/T*
-1
-0.5
0
0.5
1
1.5
2
2.5
3
Dimensionless quantity

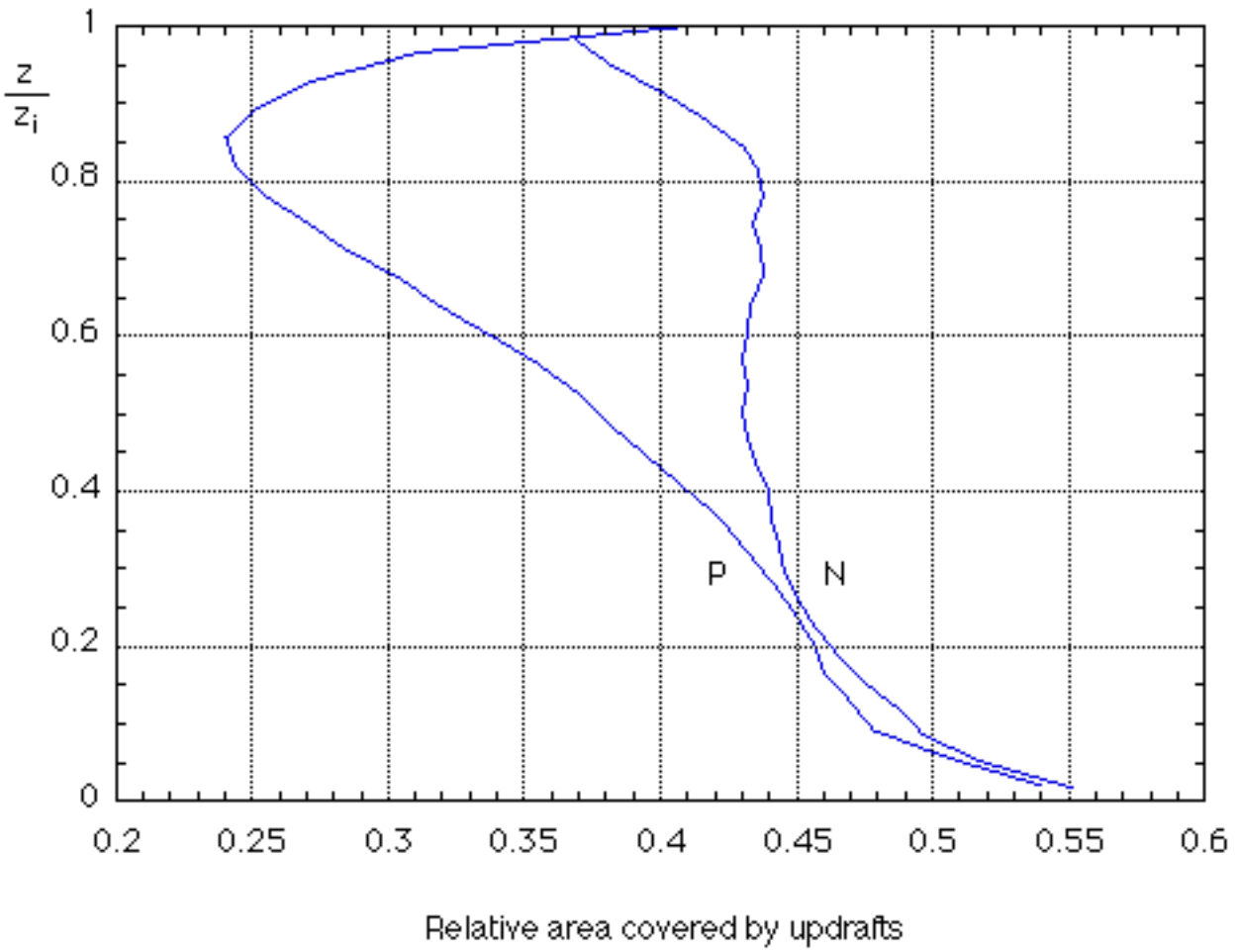
z/zi
1
0.8
0.6
0.4
0.2
0
0.2
0.25
0.3
0.35
0.4
0.45
0.5
0.55
0.6
P
N
Relative area covered by updrafts

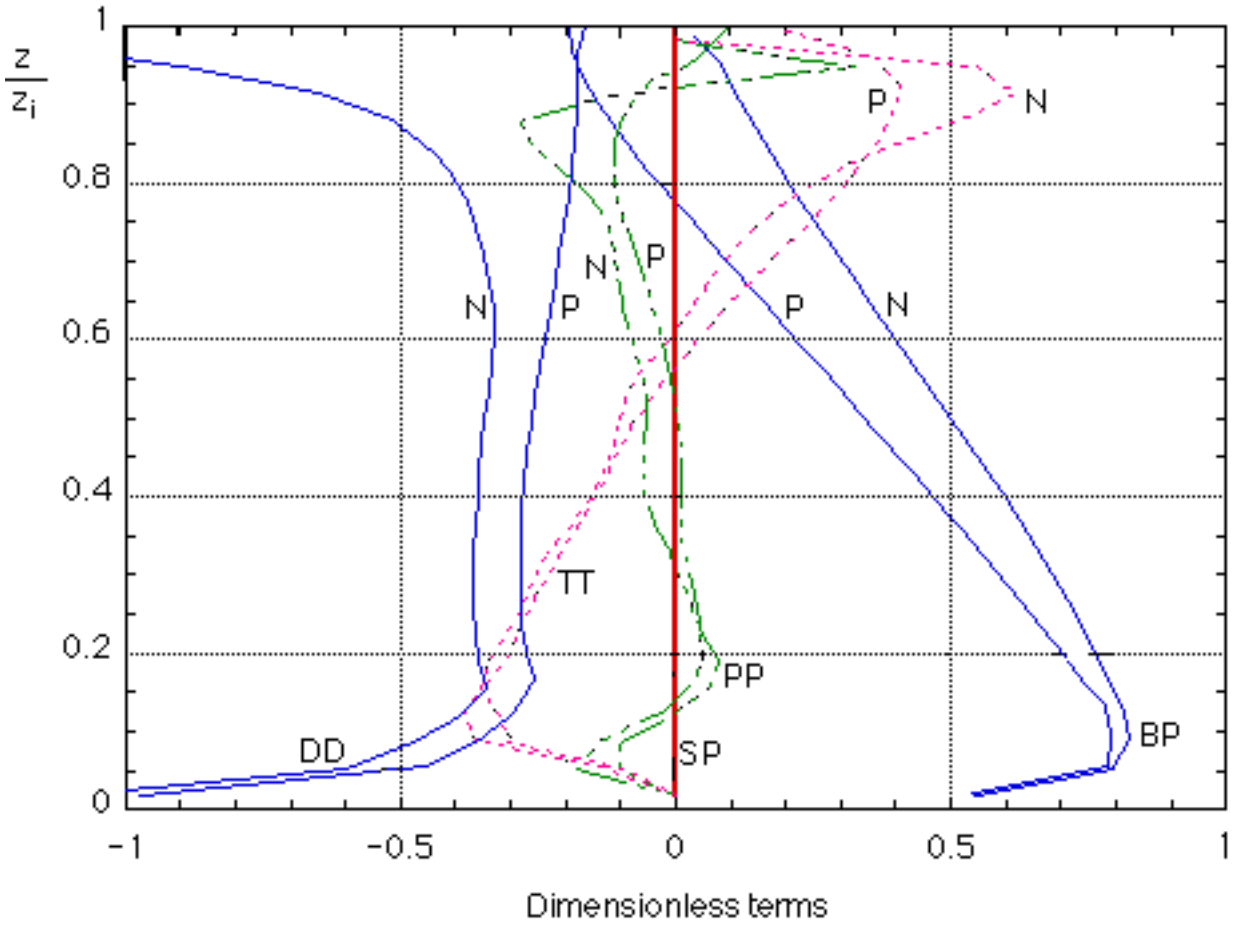
z/zi
1
0.8
0.6
0.4
0.2
0
-1
-0.5
0
0.5
1
Dimensionless terms
N
P
N
P
N
P
P
N
TT
PP
SP
DD
BP

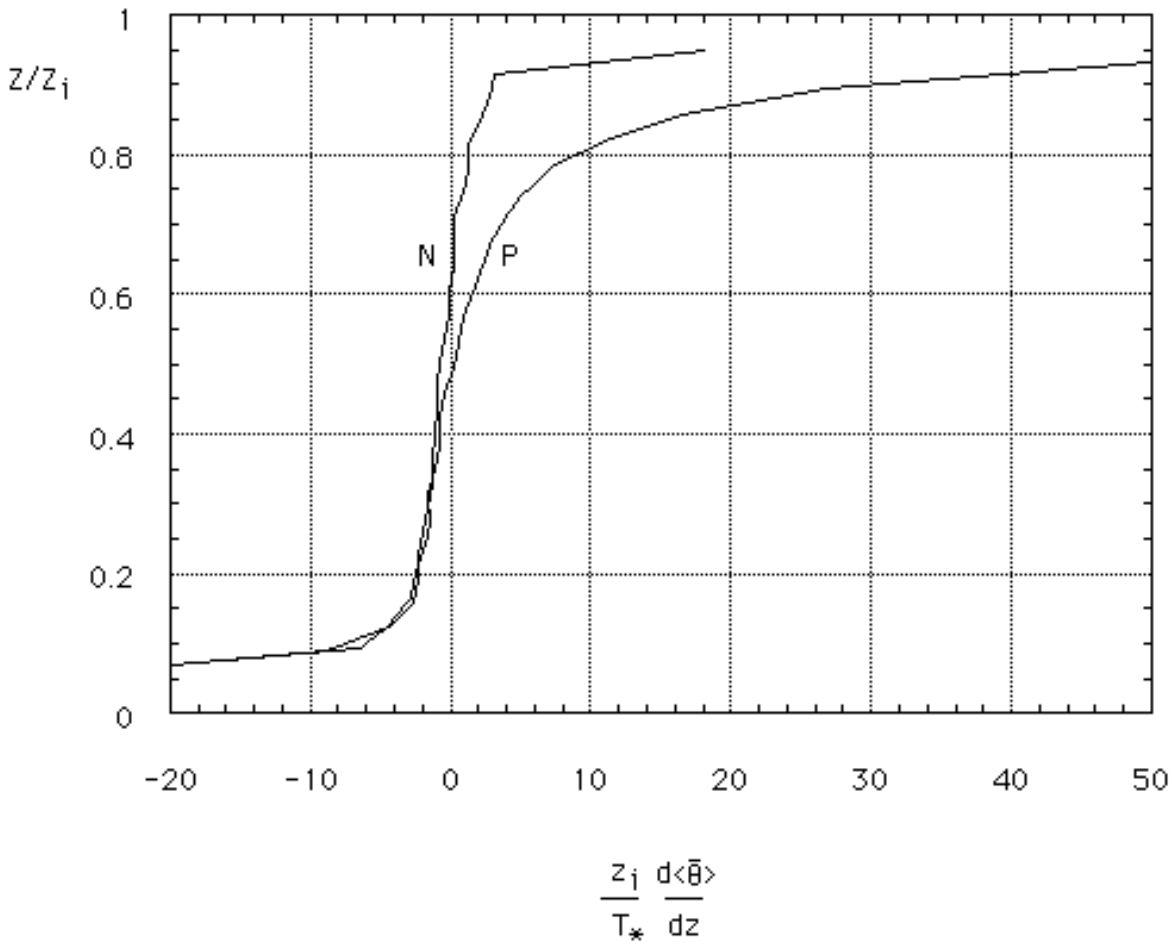
z/z_i
1
0.8
0.6
0.4
0.2
0
N
P
-20
-10
0
10
20
30
40
50
z_i / T_* d<θ̄>/dz

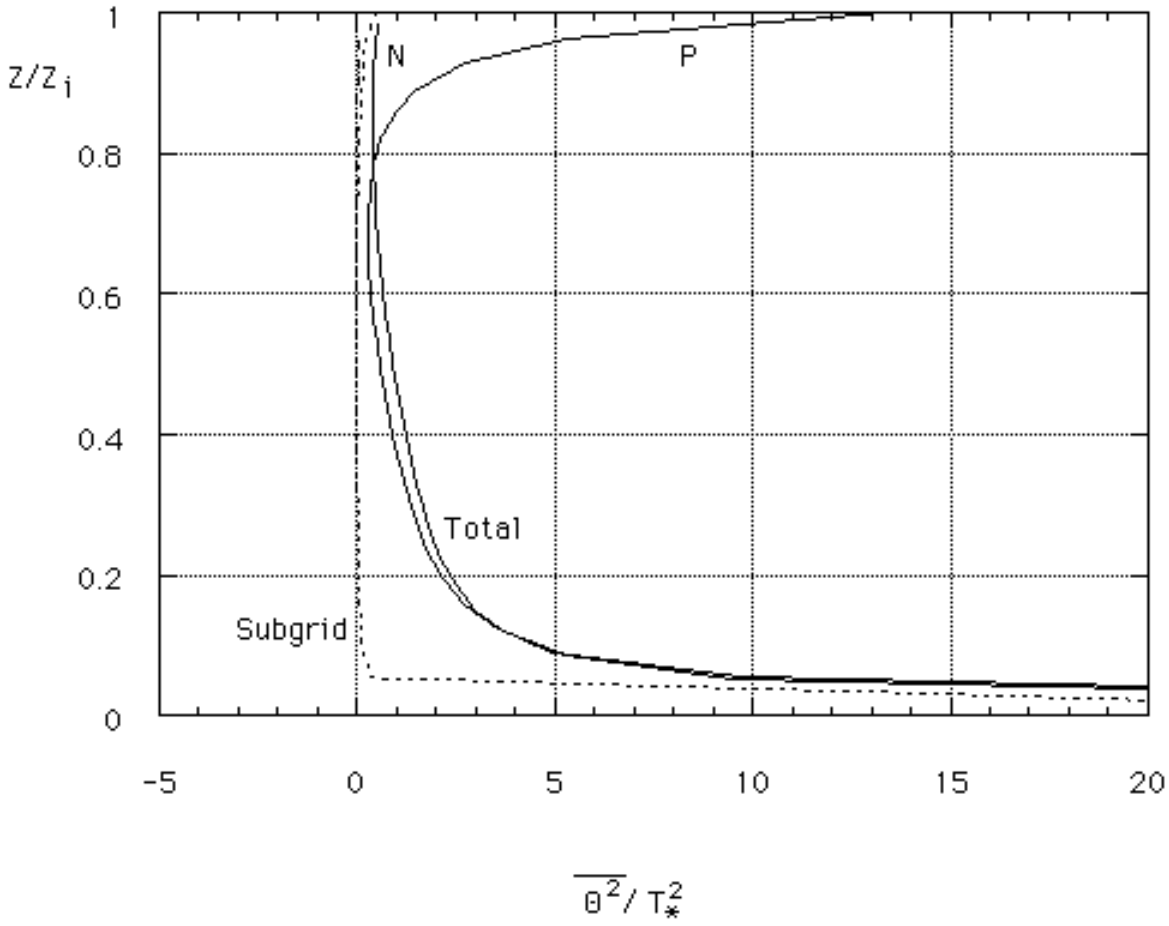
1
0.8
0.6
0.4
0.2
0
Z/Z_i
N
P
Total
Subgrid
-5
0
5
10
15
20
$\overline{\theta^2}/T_*^2$

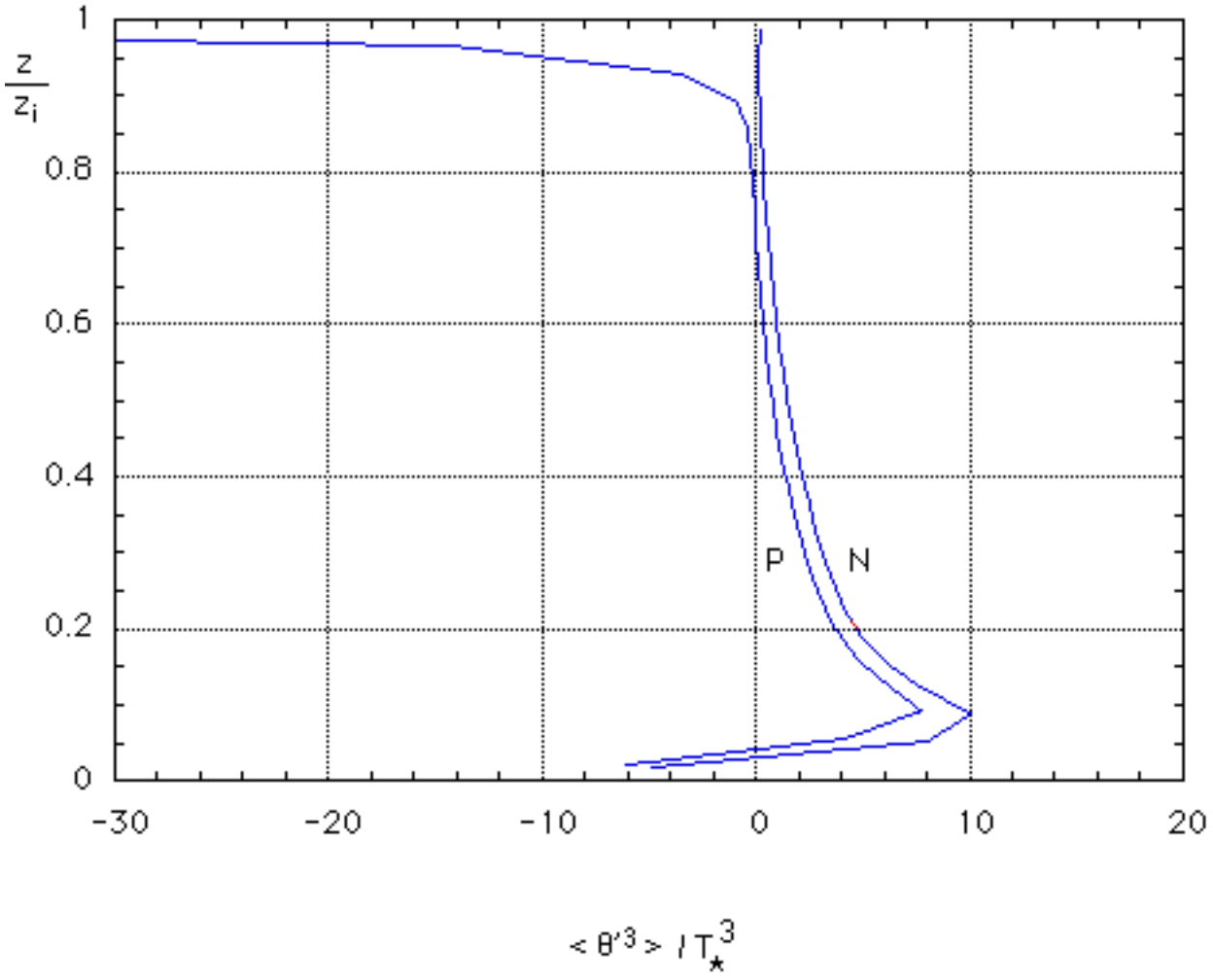
z / z_i
1
0.8
0.6
0.4
0.2
0
-30
-20
-10
0
10
20
P
N
< θ'^3 > / T_*^3

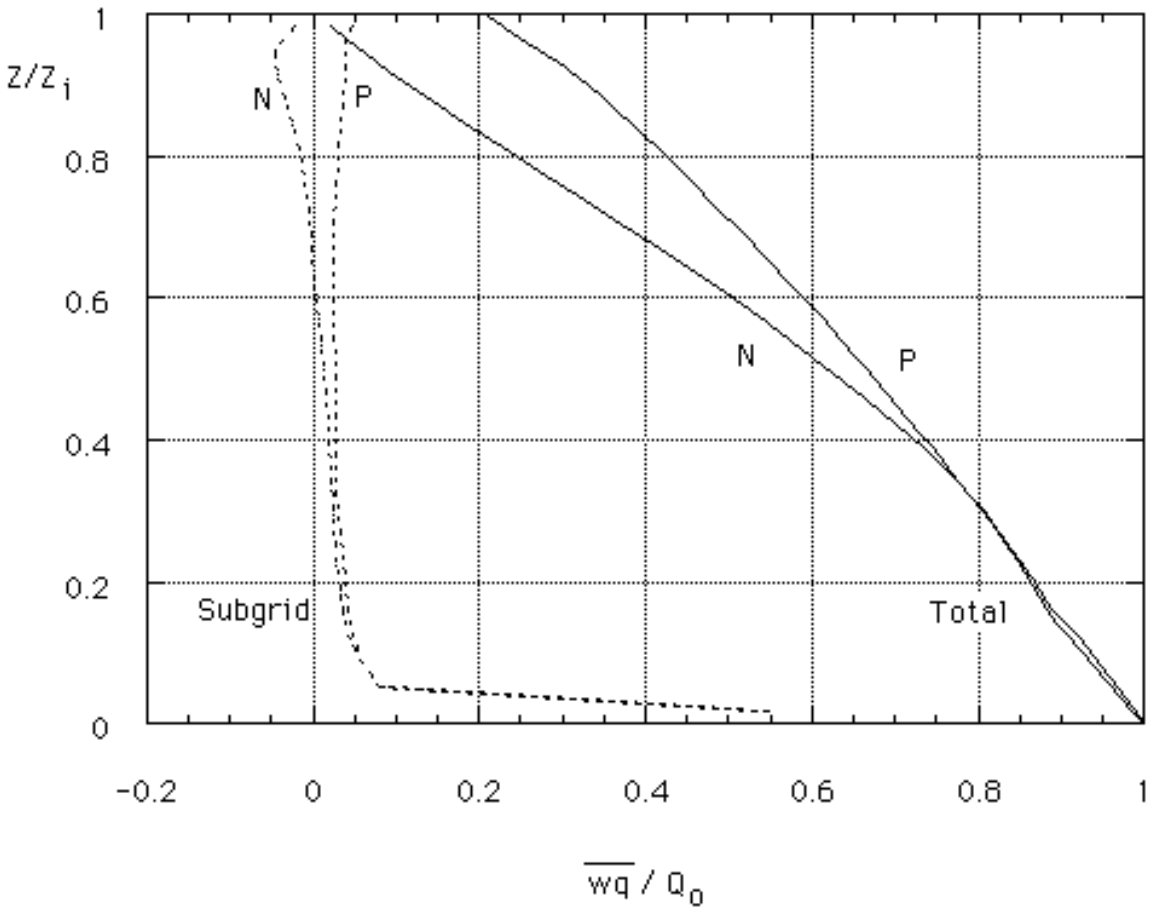
1
Z/Z i
0.8
0.6
0.4
0.2
0
N
P
N
P
Subgrid
Total
-0.2
0
0.2
0.4
0.6
0.8
1
wq / Q0

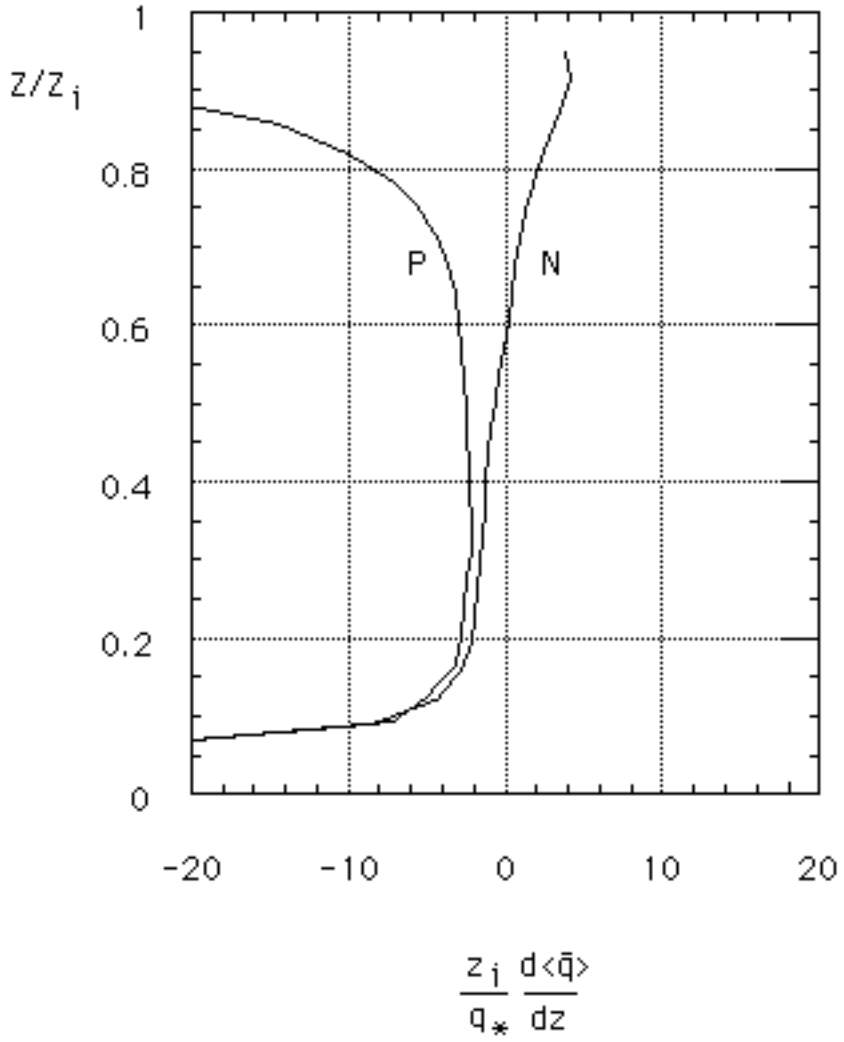
z/z_i
1
0.8
0.6
0.4
0.2
0
P
N
-20
-10
0
10
20
z_i / q_* d<q̄>/dz

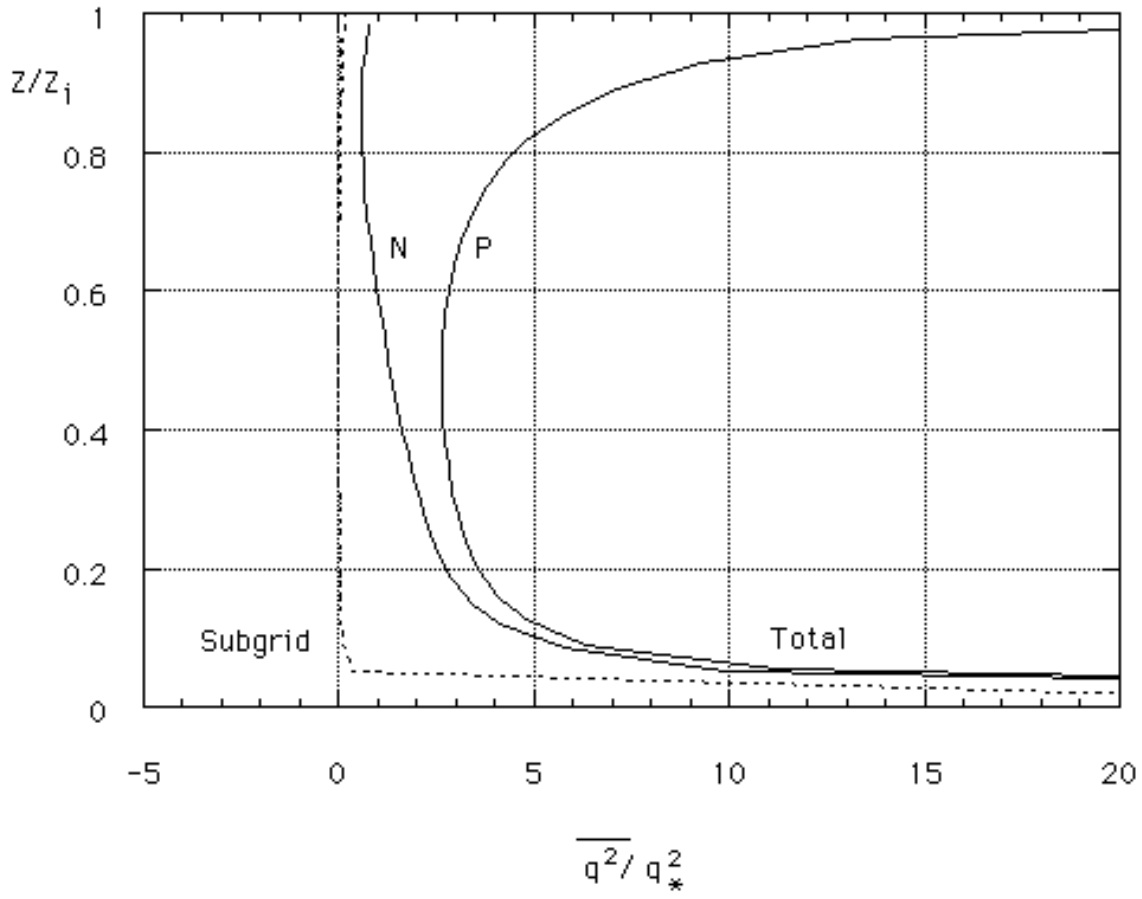
1
z/z_i
0.8
0.6
0.4
0.2
0
N
P
Subgrid
Total
-5
0
5
10
15
20
$\overline{q^2}/q_*^2$

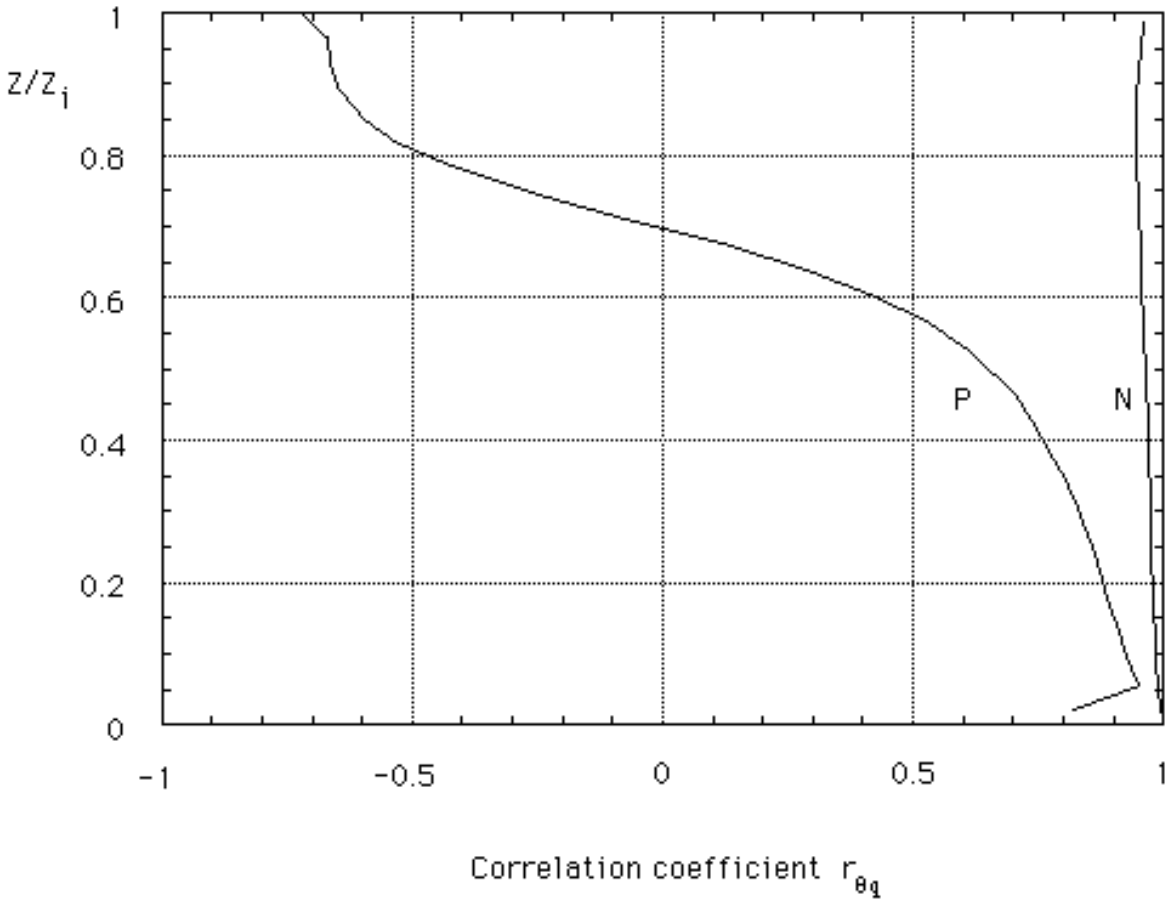
1
0.8
0.6
0.4
0.2
0
z/z_i
P
N
-1
-0.5
0
0.5
1
Correlation coefficient r_θq

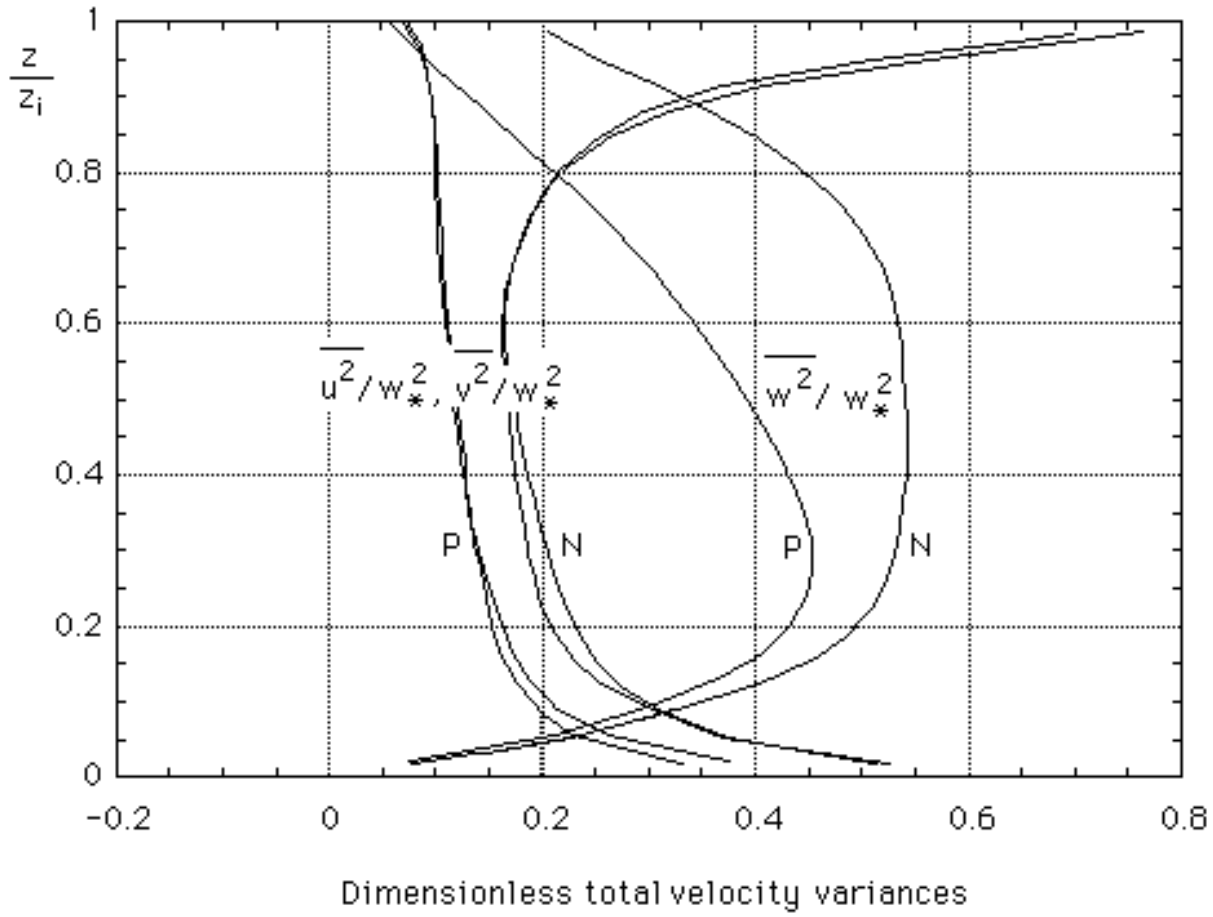
z/z_i
1
0.8
0.6
0.4
0.2
0
-0.2
0
0.2
0.4
0.6
0.8
u²/w*², v²/w*²
w²/w*²
P
N
P
N
Dimensionless total velocity variances

FIGURES